Preprint

Radiometric homogenisation of aerial images by calibrating with satellite data

Dugal Harris
Adriaan van Niekerk

Published paper:

https://doi.org/10.1080/01431161.2018.1528404

Source code:

https://github.com/dugalh/homonim

Cite as:

Harris, Dugal, and Adriaan van Niekerk. 2019. "Radiometric Homogenisation of Aerial Images by Calibrating with Satellite Data." *International Journal of Remote Sensing* 40 (7). Taylor & Francis: 2623–47. doi:10.1080/01431161.2018.1528404.

Radiometric homogenisation of aerial images by calibrating with satellite data

Dugal Harris [a] & Adriaan van Niekerk [b]

[a] *Department of Geography and Environmental Studies, Stellenbosch University, Stellenbosch 7602, South Africa, (email: dugalh@gmail.com, tel: +27 82 843 9679, postal address: PO Box 180, Newlands, Cape Town, 7725)*

[b] *Centre for Geographical Analysis, Stellenbosch University, Stellenbosch 7602, South Africa, (email: avn@sun.ac.za, tel: +27 21 808 3101, postal address: Private Bag X1, Matieland, Stellenbosch, 7602)*

Corresponding author: Dugal Harris

Radiometric homogenisation of aerial images by calibrating with satellite data

The use of very high resolution (VHR) aerial imagery for quantitative remote sensing has been limited by unwanted radiometric variation over temporal and spatial extents. In this paper we propose a simple yet effective technique for the radiometric homogenisation of the digital numbers of aerial images. The technique requires a collocated and concurrent, well-calibrated satellite image as surface reflectance reference to which the aerial images are calibrated. The bands of the reference satellite sensor should be spectrally similar to those of the aerial sensor. Using radiative transfer theory, we show that a spatially varying local linear model can be used to approximate the relationship between the surface reflectance of the reference image and the digital numbers of the aerial images. The model parameters for each satellite pixel location are estimated using least squares regression inside a small sliding window. The technique was applied to a set of aerial images captured over multiple days with an Intergraph Digital Mapping Camera (DMC) system. A near-concurrent Moderate Resolution Imaging Spectroradiometer (MODIS) nadir bidirectional reflectance distribution function (BRDF) adjusted reflectance image was used as the reflectance reference dataset. The resulting DMC mosaic was compared to a near-concurrent Satellite Pour l'Observation de la Terre (SPOT) 5 reflectance image of a portion of the same area, omitting the blue channel from the DMC mosaic due to its absence in the SPOT 5 data. The mean absolute reflectance difference was found to be 3.43% and the mean coefficient of determination (R^2) over the bands was 0.84. The technique allows the production of seamless mosaics corrected for coarse scale atmospheric and BRDF effects and does not require the manual acquisition (or provision) of ground reflectance references. The accuracy of corrections is limited by the resolution of the reference image, which is generally significantly coarser than VHR imagery. The method cannot correct for small scale BRDF or other variations not captured at the reference resolution. Nevertheless, results show a significant improvement in homogeneity and correlation with SPOT 5 reflectance.

Keywords: aerial images; radiometric calibration; surface reflectance; BRDF correction; atmospheric effects; mosaic

1 Introduction

Very high resolution (VHR) aerial and drone imagery is increasingly being used in remote sensing studies. The high spatial resolution of these images enables analyses on a finer spatial scale than most satellite-based platforms can provide and consequently allows the exploitation of information such as texture, object-based features and unmixed pixel spectra that is not available in lower resolution images (Markelin et al. 2012; Collings et al. 2011; López et al. 2011; Chandelier and Martinoty 2009; Honkavaara et al. 2009). Accurate geometric calibration techniques for producing orthorectified images are well established and form part of typical aerial imagery processing workflows (Chandelier and Martinoty 2009). Because aerial image mosaics are commonly produced for the purpose of visual interpretation, techniques such as dodging and lookup tables (LUTs) are often used to produce smooth and visually appealing results (López et al. 2011). This kind of adjustment can damage the spectral information content and is not suited to quantitative remote sensing. Also, spatial and temporal radiometric variations in aerial imagery limit the spatial and temporal extents to which quantitative remote sensing techniques can be successfully applied (Markelin et al. 2012). Ideally, quantitative analyses should be carried out on reflectance values. Atmospheric influences, bidirectional reflectance distribution function (BRDF) effects and sensor variations all contribute to radiometric variations in the imagery. To obtain surface reflectance, these radiometric variations must be removed, or reduced as far as possible. Transformation to surface reflectance is beneficial, as, unlike at-sensor quantities or surface radiance, surface reflectance is invariant to changes in atmospheric conditions and viewing geometry. This allows the surface reflectance data to be used in physical models, fused with other reflectance data and used in multi-temporal studies (Downey et al. 2010; Vicente-Serrano, Pérez-Cabello, and Lasanta 2008).

There is some confusion and ambiguity around the use of reflectance terminology in the literature (Schaepman-Strub et al. 2006). In this paper, 'surface reflectance' is used to refer to the nadir BRDF-adjusted reflectance (NBAR) measurement provided by the Moderate Resolution Imaging Spectroradiometer (MODIS) MCD43 BRDF/albedo products. NBAR is the bidirectional reflectance factor normalised to local solar noon and viewed at nadir. It is worth noting that it is not possible or practical to correct for all the sources of radiometric variation in aerial imagery. The surface reflectance in most so-called 'corrected' or 'calibrated' images is only an approximation of the actual value.

A number of techniques for the correction of BRDF effects are available, including the popular kernel-based method (Roujean, Leroy, and Deschamps 1992). Approaches based on radiometric transfer modelling, such as Atmospheric/Topographic Correction (ATCOR) (Richter 1997), Moderate Resolution Atmospheric Transmission (MODTRAN) (Berk et al. 1999) and Second Simulation of a Satellite Signal in the Solar Spectrum (6S) (Vermote et al. 1997) are used for atmospheric correction. While these atmospheric and BRDF correction methods are effective on single images (Markelin et al. 2012), blocks of multiple aerial images present unique challenges. The large field of view of aerial imaging cameras causes the viewing geometry to vary significantly within images (Lelong et al. 2008). Aerial campaigns are usually carried out over multiple days, resulting in significant variation in BRDF and atmospheric conditions. Each land cover also has its own unique BRDF and corrections should ideally model each of these covers separately (Collings et al. 2011; Honkavaara et al. 2009). Aerial campaigns can also consist of thousands of images, making it impractical to apply time-consuming atmospheric and BRDF correction models to every image (López et al. 2011). Even if it was practical, remnant radiometric variation due to the

inexact nature of BRDF and atmospheric corrections will result in discontinuities, or seam lines, between adjacent images (S. Gehrke and Beshah 2016).

Approaches to calibrating mosaics of aerial imagery are receiving increasing attention (Chandelier and Martinoty 2009; Downey et al. 2010; Collings et al. 2011; López et al. 2011; S. Gehrke and Beshah 2016). Collings et al. (2011) introduced an empirical spatially varying model to perform combined atmospheric and BRDF correction. Land cover is assumed uniform in each image, resulting in a per-image BRDF parameterisation. The parameters of the model are solved by minimising a cost function that considers the internal accuracy of each image, similarity of overlapping image regions and smoothness (i.e. the lack of seam lines) of the mosaic. In a second stage the entire mosaic is calibrated to absolute reflectance using specially placed ground targets with known reflectance. In Chandelier and Martinoty (2009) a simple semi-empirical three parameter model of combined atmospheric and hot spot BRDF effects is fitted for each image by minimising the difference between 'radiometric tie-points', a selection of points in the overlapping image regions. It is a relative calibration method and no adjustment to absolute reflectance is made. López et al. (2011) apply theoretical atmospheric and semi-empirical BRDF kernel models using field-acquired spectral data. Gehrke (2010) uses standard atmospheric and BRDF methods, followed by a relative radiometric normalisation step using invariant points in overlapping regions to smooth the mosaic. A new radiometric normalisation method for heterogeneous image data, presented in Gehrke and Beshah (2016), improves on that of Gehrke (2010). The shortcomings of existing atmospheric and BRDF image adjustments are corrected using a spatially varying linear model. Model parameters are found at points in overlapping image regions and then interpolated into the remainder of the images.

A disadvantage of the aerial mosaic calibration techniques described above is their complexity and need for known ground references to achieve transformation to absolute surface reflectance. A number of the techniques also assume uniform BRDF characteristics within an image (Collings et al. 2011; Chandelier and Martinoty 2009; López et al. 2011). The options of placing targets of known reflectance to be captured as part of the mosaic or measuring the reflectance of suitably invariant sites on the ground are often not possible or practical. Many applications make use of archived imagery that had been captured prior to the commencement of the research and for which concurrent ground measurements are consequently not possible. Another approach is to make use of vicarious calibration involving knowledge of the spectral characteristics of specific ground sites, but this is recognised as being labour-intensive and costly (Gao et al. 2013; Chander, Meyer, and Helder 2004; Liu et al. 2004).

In this paper, we propose a method of homogenising aerial imagery to coarse scale surface reflectance by calibrating to a concurrent and collocated satellite image that has been corrected for atmospheric and BRDF effects. Satellite programmes such as MODIS make such coarse-resolution surface reflectance products freely available. The proposed method avoids the need to perform atmospheric and BRDF corrections explicitly. It also does not require the placement of known reflectance targets or field spectral measurements, which can be impractical, error-prone and time-consuming in many instances. The technique was applied to a large set of aerial images captured with an Intergraph Digital Mapping Camera (DMC). A near-concurrent MODIS MCD43A4 NBAR product was used as the reflectance reference dataset. The resulting DMC mosaic was compared to a near-concurrent Satellite Pour l'Observation de la Terre (SPOT) 5 reflectance image of the same area.

2 Methods

2.1 Formulation of the Local Linear Model

The proposed method is based on approximating combined BRDF, atmospheric and sensor effects as a spatially varying linear relationship between surface reflectance and sensor measurement. Similar local linear relationships are used by Chandelier and Martinoty (2009), Collings et al. (2011) and Gehrke and Beshah (2016) for the radiometric correction of aerial image mosaics. In this section, we show that a spatially varying linear model is supported by radiative transfer theory.

Following the notation of López et al. (2011), the digital number (DN) measurement of an aerial sensor for each band can be expressed as:

$$\mathrm{DN} = c_0 L_\mathrm{s} + c_1 \tag{1}$$

where L_s is the radiance at the sensor and c_0 and c_1 are coefficients determined by the characteristics of the sensor. The proposed method requires the sensor radiance response to be linear; it should first be corrected for any non-linearity where this is not the case. The radiance at the sensor is expressed as:

$$L_\mathrm{s} = \frac{\rho_\mathrm{s} E_\mathrm{s} \cos\theta}{\pi} \tag{2}$$

where ρ_s is the reflectance at the sensor, E_s is the irradiance at the sensor, and θ is the solar zenith angle. The reflectance of a uniform Lambertian surface at the sensor is described by the radiative transfer equation (Vermote et al. 2006):

$$\rho_s = \rho_a + \frac{\rho_t}{1 - S\rho_t} \tau_u \tau_d \tau_g \quad (3)$$

where ρ_a is the intrinsic atmospheric reflectance, ρ_t is the surface reflectance and S is the atmospheric albedo. τ_u and τ_d are the atmospheric transmittances due to molecular and aerosol scattering between the surface and sensor and between the sun and the surface respectively, and τ_g is the global atmospheric transmittance due to molecular absorption. It is common for aerial surveys to be conducted on clear days (Chandelier and Martinoty 2009). This was the case for the imagery used in our study. In clear sky conditions, the atmospheric albedo, S, is typically around 0.07 (Manabe and Strickler 1964). With a small value for S and a maximum value of one for ρ_t, the denominator in Equation (3) is approximately one and the reflectance at the sensor can be approximated as:

$$\rho_s \simeq \rho_a + \rho_t \tau_u \tau_d \tau_g \quad (4)$$

Equations (1), (2) and (4) express the relationship between the sensor measurement, atmospheric conditions and the surface reflectance. With the approximation of Equation (4), there is a linear relationship between surface reflectance and the sensor measurement. This linear relationship can be expressed as:

$$\mathrm{DN} = M\rho_t + C \quad (5)$$

where

$$M = \frac{1}{\pi} c_0 \tau_u \tau_d \tau_g E_s \cos\theta \quad (6)$$

and

$$C = c_1 + \frac{1}{\pi} c_0 \rho_a E_s \cos\theta \quad (7)$$

The parameters M and C are spatially varying functions of the viewing geometry and atmospheric conditions. Implicit in any radiometric calibration technique is an approximation of these parameters so that the relationship can be inverted. A discussion of pertinent model assumptions is provided in the following section.

2.2 Parameter Estimation

In our proposed method, we solve for M and C of the aerial sensor using a reference estimate for the surface reflectance parameter, ρ_t^{ref}, obtained from a well-calibrated satellite image. The reference surface reflectance image should have been captured at a similar time to the uncalibrated aerial image(s). The spatially varying property of the model allows the reduction of atmospheric effects that vary during aerial campaigns. The time difference between the reference and uncalibrated aerial images should, however, be small enough to avoid phenological or structural land cover changes. Such changes cannot be accounted for by the proposed method and will lead to errors (local to the area of change) in the calibrated result. In this study we use a 16 day composite reference image comprised of data from 25 January to 9 February 2010 and aerial images captured over multiple days between 22 January and 8 February 2010.

Least squares estimates of M and C, for the aerial sensor, are found for each pixel of the reference image inside a sliding window. Equation (5) can be rewritten in vector form, using the reference surface reflectance, ρ_t^{ref}, for the pixels inside a sliding window.

$$\boldsymbol{DN} = M\boldsymbol{\rho}_{\mathrm{t}}^{\mathrm{ref}} + C\boldsymbol{1} \tag{8}$$

where $\boldsymbol{\rho}_{\mathrm{t}}^{\mathrm{ref}}$ and $\boldsymbol{DN}$ are column vectors of the N values inside the sliding window and $\boldsymbol{1}$ is a column vector of ones of length N. $\boldsymbol{\rho}_{\mathrm{t}}^{\mathrm{ref}}$ is obtained from the reference image and $\boldsymbol{DN}$ from the uncalibrated aerial image(s). The parameters can then be estimated as follows:

$$\begin{bmatrix} M \\ C \end{bmatrix} = [\boldsymbol{\rho}_t^{ref} \quad \boldsymbol{1}]^{-1}(\boldsymbol{DN}) \tag{9}$$

In this form, the sliding window should consist of at least two pixels to solve for the two parameters. In order to accommodate the differing spatial resolutions, M and C must be found at the reference spatial resolution, resampled to the aerial spatial resolution, and then used to estimate surface reflectance at this resolution by inverting the relationship of Equation (5). The choice of the sliding window size involves a trade-off between the accuracy and effective spatial resolution of the estimated radiometric correction parameters, *M* and *C*. In essence, it is the typical parameter estimation trade-off between bias and variance or under- and over-fitting (Webb 2002). Larger sliding windows will be less susceptible to over-fitting on noisy data, while smaller sliding windows will provide higher spatial resolution correction parameters. The choice of sliding window size for the case study is discussed in Sections 2.5 and 3.4, and the effect of varying the sliding window size is investigated in Section 3.4.

The reference image will typically be at a substantially lower spatial resolution than the aerial imagery. BRDF corrected surface reflectance products, such as those produced from MODIS and Multi-angle Imaging SpectroRadiometer (MISR), have resolutions of the order of 500 m while aerial images usually have resolutions of 2 m or higher. This large

resolution discrepancy affects the accuracy of the results. While the Equation (5) model applies to an aerial pixel, *M* and *C* are estimated at the reference resolution before resampling them to the aerial resolution. The reference resolution is only sufficient to capture gradual changes in BRDF and atmospheric conditions. Real BRDF can vary significantly over short distances where land cover is heterogeneous. This type of small scale BRDF variation is not captured at the resolution of the reference image and cannot be corrected for by the method. The theoretical formulation of Section 2.1 is intended to lend support to the use of the local linear model. It is acknowledged that the model involves a number of approximations and simplifications. These include ignoring adjacency effects and BRDF coupling with atmospheric effects (Vermote et al. 2006). We regard these approximations as necessary limitations of the method. Related methods make similar assumptions about BRDF homogeneity, often assuming a per-image BRDF model (Collings et al. 2011; Chandelier and Martinoty 2009; López et al. 2011) and also using simplified local linear models for approximating radiative transfer (Chandelier and Martinoty 2009; Collings et al. 2011; S. Gehrke and Beshah 2016).

2.3 Incorporation of Viewing Geometry and Relative Spectral Response Effects

The formulation of the local linear model in section 2.1 does not consider the effect of viewing geometry and relative spectral response (RSR) differences between the aerial and reference images. In this section, we show that these effects can also be modelled as locally linear relations, which can then be combined with Equation (5) to form a single linear relation between ρ_t^{ref} of the reference image and DN of the uncalibrated aerial image(s). These combined effects are thus still approximated by a spatially varying linear model with parameters as estimated with Equation (9).

The surface reflectance in Equation (4) represents the simplified case of a Lambertian reflector (i.e. it reflects equally in all directions), but in practice is subject to BRDF effects and so also varies with the viewing geometry (i.e. spatially) as in Equation (10).

$$\rho_{\mathrm{t}} = f(\xi) \tag{10}$$

where f is the BRDF and $\xi = (\theta, \vartheta, \phi)$ is the viewing geometry, θ is the solar zenith angle, ϑ is the view zenith angle and ϕ the relative azimuth. To incorporate BRDF into the model, it is necessary to account for the viewing geometry differences between the reference and aerial images. It is not valid to simply replace the unknown aerial surface reflectance with the reference surface reflectance in Equation (5) when they occur at different viewing geometries. To describe the relationship between the two reflectances at a particular location, we express their ratio in Equation (11).

$$\frac{\rho_{\mathrm{t}}^{\mathrm{aerial}}}{\rho_{\mathrm{t}}^{\mathrm{ref}}} = \frac{f(\xi^{\mathrm{aerial}})}{f(\xi^{\mathrm{ref}})} \tag{11}$$

Here $\rho_{\mathrm{t}}^{\mathrm{aerial}}$ and $\rho_{\mathrm{t}}^{\mathrm{ref}}$ are the aerial and reference surface reflectances respectively, and ξ^{aerial} and ξ^{ref} are the aerial and reference viewing geometries respectively. The aerial surface reflectance can then be expressed as a multiple of the reference surface reflectance.

$$\rho_{\mathrm{t}}^{\mathrm{aerial}} = \frac{f(\xi^{\mathrm{aerial}})}{f(\xi^{\mathrm{ref}})}\rho_{\mathrm{t}}^{\mathrm{ref}} = F\rho_{\mathrm{t}}^{\mathrm{ref}} \tag{12}$$

F is a spatially varying function of the aerial and reference viewing geometries. As this relation is locally linear, it can be incorporated into the model of Equation (5), maintaining the linearity and spatially varying properties. Coupling between atmospheric and

BRDF effects (Vermote et al. 2006) are not included in the model. The parameter *F* of Equation (12) is effectively estimated at the reference image resolution. The effects of viewing angle variations at the aerial image resolution are approximated by interpolating the coarse scale homogenisation parameters to the aerial resolution.

The model presentation in Section 2.1, ignored the effect of the spectral responses of the reference and uncalibrated sensors. The relation between surface reflectance and sensor measurement in Equation (5) becomes non-linear when including the spectral response effect. The surface reflectance in Equation (5) is a band averaged quantity, as represented by Equation (13).

$$\rho_{\mathrm{t}} = \frac{\int \rho_{\mathrm{t}}(\lambda) R(\lambda) \mathrm{d}\lambda}{\int R(\lambda) \mathrm{d}\lambda} \tag{13}$$

where $\rho_{\mathrm{t}}(\lambda)$ is the spectral surface reflectance and $R(\lambda)$ is the sensor RSR for a particular band. Without knowledge of the surface reflectance spectra, it is not possible to completely calibrate for this effect. However, for real world surface reflectances it can often be shown that the relationship between the band averaged values for different sensors is approximately linear (Gao et al. 2013; Jiang and Li 2009). This means the relationship between surface reflectance and sensor measurement remains approximately linear even when the sensor spectral response is considered. We therefore approximate the effect of sensor spectral responses as a locally linear relationship that is incorporated into the linear model of Equation (5). This approximation is supported by simulations for the case study sensors in Sections 2.6 and 3.1.

2.4 Surface Reflectance Homogenisation

The homogenisation procedure follows these steps:

(1) Resample uncalibrated aerial images to the reference image resolution and grid.

(2) With the output from step (1), calculate sliding window estimates of M and C for each pixel of each band of the reference image using Equation (9). This forms two multi-band rasters **M** and **C** at the reference grid and resolution.

(3) Resample **M** and **C** rasters to the aerial image resolution and grid.

(4) Calculate estimated surface reflectance for each pixel of each band of the uncalibrated aerial image, using Equation (5).

The choice of resampling algorithms in steps 1 and 3 of the procedure are important, especially when there is a large difference in the spatial resolution of the aerial and reference images. Optical imaging systems are linear and thus subject to the superposition principle, which manifests as spectral mixing (Akhmanov and Nikitin 1997). Averaging the uncalibrated image over each reference pixel area is recommended when downsampling in step 1. This will approximate the spectral mixing that occurs in the larger reference image pixels.

It is necessary to produce smooth **M** and **C** rasters in step 3 to approximate slowly varying atmospheric and BRDF effects and to avoid discontinuities in the final image(s). Of the standard interpolation algorithms, cubic spline interpolation, with its constraints of continuity of the first and second derivatives, best satisfies this requirement (Hou and Andrews 1978). The Geospatial Data Abstraction Library (GDAL) (GDAL Development Team 2014) was used for implementing the resampling.

Since adjacent aerial images are calibrated to match the same reference image, overlapping image areas are similar. Blocks of aerial surface reflectance images generated with the procedure outlined above can generally be mosaicked without the need for additional colour balancing or normalisation procedures to reduce seam lines. Due to the disparity between reference and aerial image resolutions, there may be situations (such as uneven, shadowed terrain) where fine scale differences between adjacent images produce slight seam lines. In these situations, one could use a feathering procedure to blend overlapping areas. In the case study however, we did not find this to be necessary.

2.5 Study Site, Data Collection and Preparation

The surface reflectance homogenisation method proposed in this paper was tested in a 96 km × 107 km area (Figure 1) in the Little Karoo in South Africa. This particular study site was chosen as the calibration work forms part of a larger vegetation mapping study being done in the area.

The Chief Directorate: National Geo-spatial Information (NGI), a component of the South African Department of Rural Development and Land Reform, acquires and supplies national coverage aerial imagery. VHR multispectral 0.5 m pixel^{-1} imagery of the study area was obtained from the NGI archive. The imagery was captured with a multispectral Intergraph DMC with red, green, blue and near-infrared (NIR) channels.

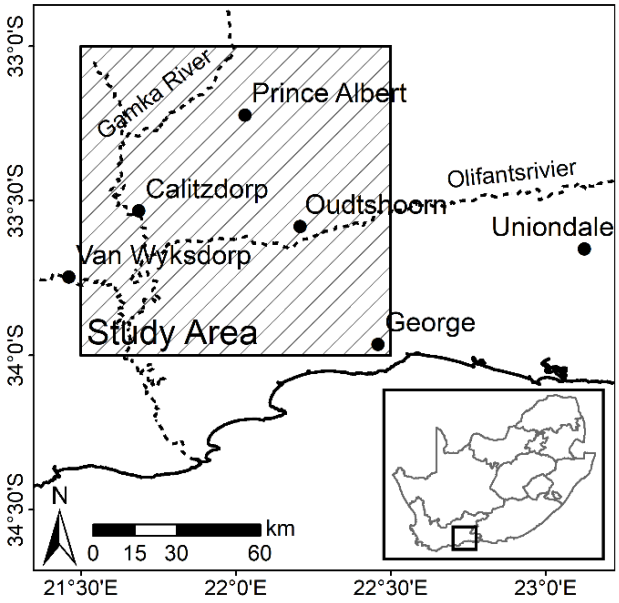

Figure 1. Study area orientation map

The RSRs of the DMC and MODIS sensors are shown in Figure 2. The peaks overlap well between the sensors in the red, green and blue bands, while the DMC NIR band is wider than that of MODIS.

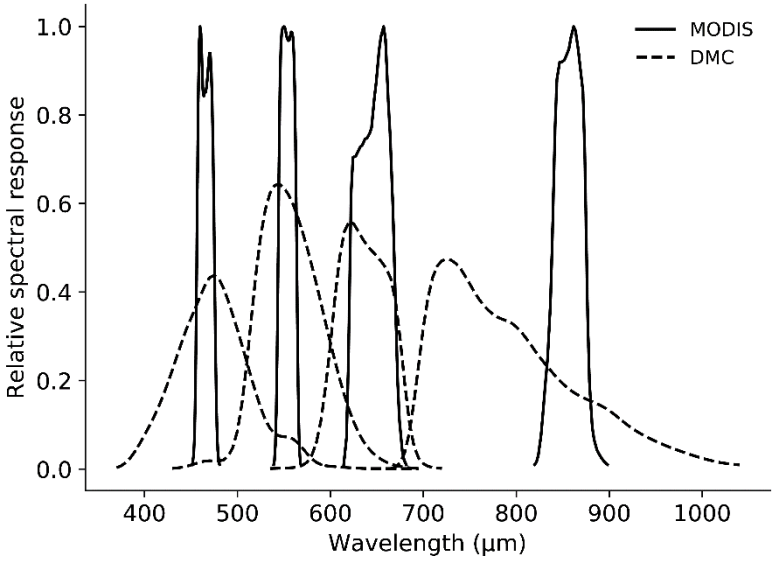

Figure 2. DMC's and MODIS's RSR

The study site is covered by 2228 images captured during four separate aerial campaigns on multiple days from 22 January 2010 to 8 February 2010. The inclusion of a large set of imagery acquired over multiple days allows an investigation into the robustness of the method to temporal variation (and the consequent BRDF and atmospheric variations). There is an average sidelap of 25% between images in adjacent flight lines and an average forward overlap of 60% between consecutive images in the same flight line. The images were captured close to nadir, with a maximum tilt of 5.0°, at a height of 5000 m above ground. The DMC has a 69.3° cross track and 42.0° along track field of view (FOV). NGI campaigns are conducted on clear days such that images are free of clouds, cloud-shadows, smoke and excessive haze. Flight times are chosen to achieve a solar altitude of at least 30.0° in order to minimise shadowing. The mean aerosol optical depth (AOD) over the campaign days was 0.02 (the AOD provided by the MODIS MOD04 product was used for this calculation).

The raw aerial imagery was corrected for lens distortion, band spatial alignment, sensor non-linearity and dark current effects using the Intergraph Z/I Post-Processing Software (PPS). The PPS corrected imagery has a linear radiance response (as required by Equation (1)), with zero offset (i.e. $c_1 = 0$). This corrected imagery was orthorectified using existing aerotriangulation data supplied by NGI and a 5 m resolution digital elevation model (DEM) (Van Niekerk 2014).

A MODIS MCD43A4 NBAR product for the period from 25 January 2010 to 9 February 2010 was selected as a reference for the homogenisation. This product has a 500 m resolution and contains NBAR data composited from the best values over a 16 day period. The MODIS NBAR data has been processed with atmospheric and BRDF correction

procedures (Strahler and Muller 1999) and is recognised as a reliable reference source for cross calibration (Gao et al. 2013; Li, Yang, and Wang 2012; Jiang and Li 2009; Liu et al. 2004). The NBAR data accuracy has been verified in a number of studies and is accurate to 'well less than 5% albedo at the majority of the validation sites' (MODIS Land Team 2014). MODIS was also selected as it has similar spectral bands to the Intergraph DMC. Bands 4, 1, 3 and 2 from the MODIS sensor were used to correspond to the red, green, blue and NIR bands from the DMC sensor respectively. While Landsat surface reflectance (Schmidt et al. 2012) could be a useful source of reference data due to its relatively high spatial resolution of 30 m, no cloud-free Landsat imagery concurrent (or near-concurrent) to the aerial imagery was available for testing in the case study.

The PPS processed imagery has zero offset, so the parameter c_1 from Equation (7) was zero and the atmospheric reflectance, ρ_a, was small as the surveys were conducted on clear days, meaning that *C* was small. For the purposes of the case study, *C* was ignored and only the gain, *M*, was estimated. With only one parameter to estimate, a sliding window of one pixel was used to achieve the best possible spatial resolution in the **M** raster. The gain-only simplification is given support by the results of Collings et al. (2011) who found the gain term in their linear model to carry the majority of the corrective effect. Nevertheless, it must be acknowledged that this is an initial approach and subsequent studies should be conducted to investigate the effects of including *C*. The blue channel in particular could benefit from the inclusion of the offset (*C*) term due to its haze sensitivity.

2.6 Linearity of Band Averaged Values

In formulating the method in Section 2.1, it was assumed that the effect of sensor RSR on

measured surface reflectance is locally linear and can be incorporated in the model of Equation (5). To investigate the validity of this assumption, MODIS and DMC band averaged values were simulated for typical surface reflectance spectra and statistically compared. Twenty surface reflectance spectra were selected from the 'soil', 'vegetation', 'water' and 'man-made' classes in the Advanced Spaceborne Thermal Emission and Reflection Radiometer (ASTER) spectral library (Baldridge et al. 2009) to represent commonly encountered land covers. Band averaged values were then simulated for these representative spectra using Equation (13), with the MODIS and DMC RSRs as shown in Figure 2.

2.7 Accuracy Assessment

Given that the DMC imagery was acquired in 2010, it was not possible to assess the accuracy of the reflectance retrieval method using ground-based spectral measures. Alternative methods for evaluating the results were consequently needed. First, the DMC DN and calibrated surface reflectance images were stitched into mosaics and the mosaics were visually compared to determine if discontinuities between adjacent images were reduced and to what extent the radiometric variations were corrected. Second, the DMC homogenised mosaic was resampled to the MODIS grid and resolution, and statistically compared to the MODIS reference image. Last, we quantitatively compared the DMC homogenised mosaic to a SPOT 5 scene, and the SPOT 5 scene to the MODIS reference image.

The 10 m resolution SPOT 5 level 1A image, acquired on 21 January 2010, covers portions of all four aerial campaigns as shown in Figure 3. The image was orthorectified using a 5 m resolution DEM (Van Niekerk 2014). The SPOT 5 DN image was converted to

surface reflectance using the ATCOR 3 method (Richter 1997). While the ATCOR 3 correction did not include explicit BRDF correction, SPOT 5 is subject to substantially lower BRDF effects than the aerial imagery due to its narrow FOV . Since the SPOT 5 sensor does not have a blue band, it was omitted from this comparison. The SPOT 5 resolution of 10 m allows the homogenised surface reflectance result to be checked at a resolution significantly closer to the aerial resolution than the reference MODIS resolution. This provides a useful check of the effect of approximating BRDF and atmospheric variations at the coarse scale of the reference image. While the MODIS comparison checks the DMC surface reflectance against the reference it was fitted to, the SPOT 5 comparison uses an independent and 'unseen' source.

To establish the relative accuracy of the corrected SPOT 5 scene, it was downsampled (by averaging) to the MODIS resolution and grid and statistically compared to the MODIS reference image using Equation (14).

$$(x, y) = \left| I^{\mathrm{CMP}}(x, y) - I^{\mathrm{SPOT}}(x, y) \right| \tag{14}$$

where I^{CMP} is the MODIS image, I^{SPOT} is the SPOT 5 image, (x, y) are the pixel co-ordinates and E is the difference image. Mean absolute difference (MAD) and root mean square (RMS) statistics were found to establish a benchmark against which similar statistics for DMC homogenised mosaic could be compared.

The DMC homogenised mosaic was then downsampled (by averaging) to the SPOT 5 resolution and grid, and statistically compared to the SPOT 5 surface reflectance image using Equation (14) with I^{CMP} as the DMC mosaic in this instance.

The image resulting from the differencing process was used to identify spatial patterns in the discrepancies between the corrected SPOT 5 image and DMC mosaic. MAD and RMS statistics were found for the image to allow comparison with the results of similar studies. In addition to the statistical evaluation, individual spectra from homogenous surfaces in the SPOT 5 surface reflectance image, and DMC homogenised and DN mosaics were compared.

The impact of the sliding window size was investigated by repeating the comparison between the SPOT 5 image and homogenised DMC mosaic with increasing sliding window sizes. A sub-section of the full study area, as shown in Figure 3, was used for the sliding window size investigation, to expedite computation times.

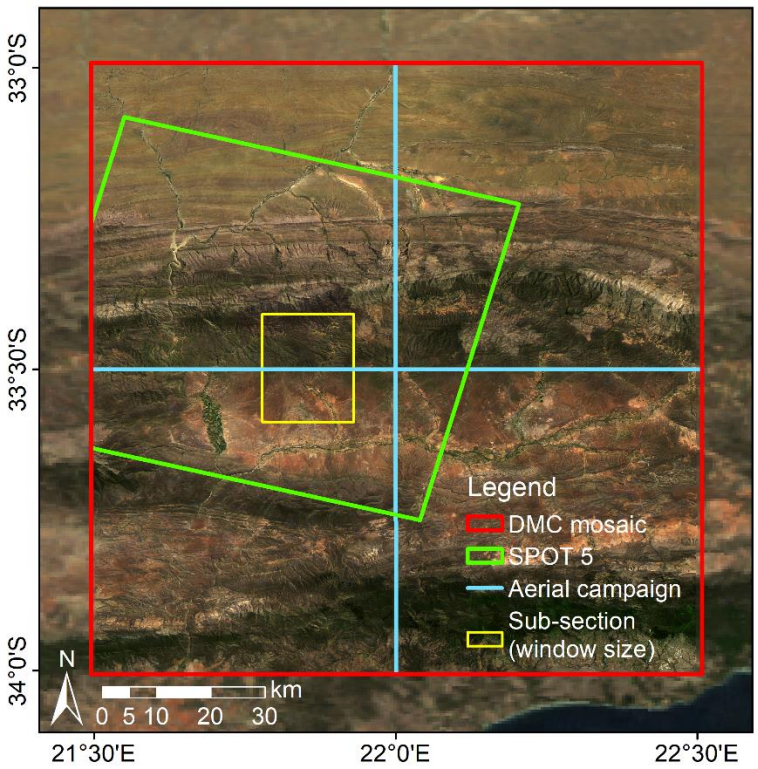

Figure 3. SPOT 5 scene and mosaic extents

3 Results and Discussion

3.1 Band Averaged Relationships

The simulated band averaged reflectance relationship for typical surface reflectances between the two sensors is shown in Figure 4 with coefficient of determination (R^2) values. The correlation between the DMC and MODIS simulated band averaged values (Figure 4) is surprisingly strong and supports the incorporation of the band averaging effect into the linear reflectance model of Equation (5). Similar linear relationships between different sensors for real world surface reflectances are reported in Gao et al. (2013) and Jiang and Li (2009). As the proposed method only requires the relationship to be locally linear, the variety of land covers simulated here is unlikely to be present inside the sliding window used to estimate the model parameters. For a small sliding window, the correlation of the band averaged values will consequently be stronger than what is shown in Figure 4. The NIR channel has the lowest R^2, likely due to the relatively larger dissimilarity between MODIS and DMC RSRs, as evidenced in Figure 2. One can consequently expect higher surface reflectance errors in this channel compared to the others.

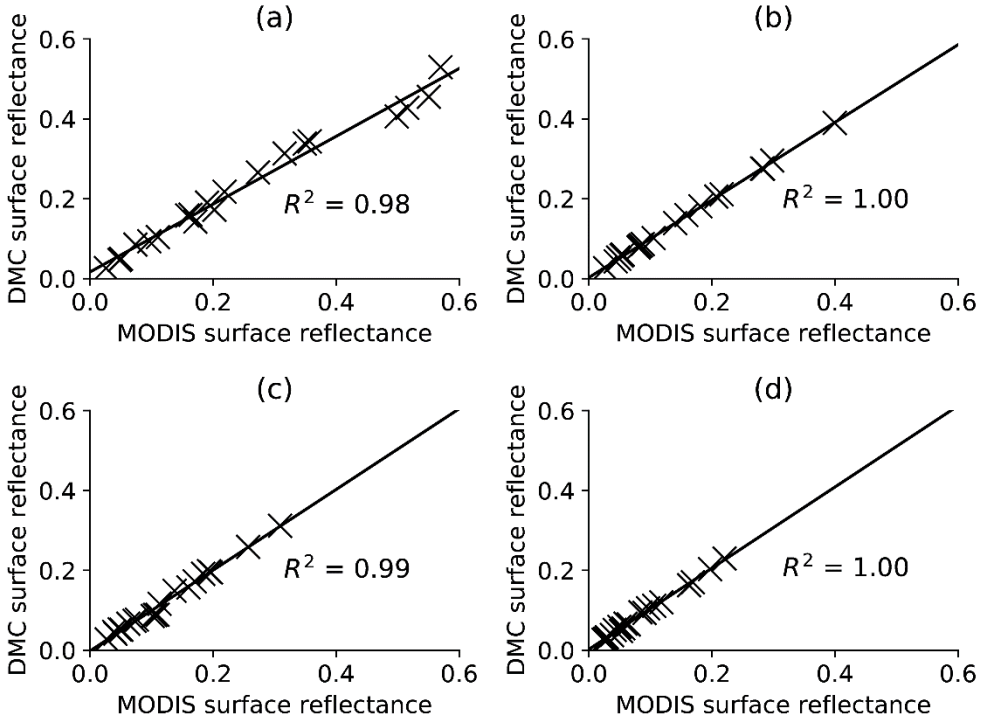

Figure 4. DMC versus MODIS simulated band averaged relationship for typical surface reflectances ((a) NIR, (b) red, (c) green and (d) blue bands)

3.2 Mosaicking

Figure 5 shows a RGB (red, green and blue) mosaic of DMC DN images (bordered in red), against a background of the MODIS reference image. Seam lines between adjacent DMC images and radiometric variations over the set of images are clearly visible.

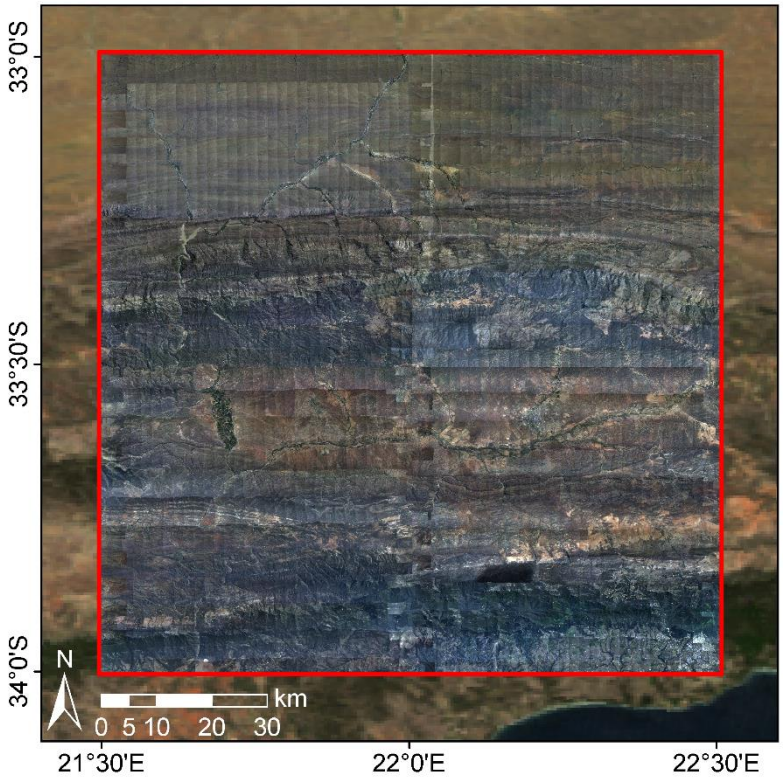

Figure 5. Uncalibrated mosaic on MODIS reference image background

Each DMC image was converted to surface reflectance using the proposed procedure. A RGB mosaic of the corrected images is shown in Figure 6, bordered in red, against a background of the MODIS reference image. No seam lines or radiometric anomalies (e.g. hot spots) are apparent at this scale, and the corrected images match the reflectance of the MODIS reference image.

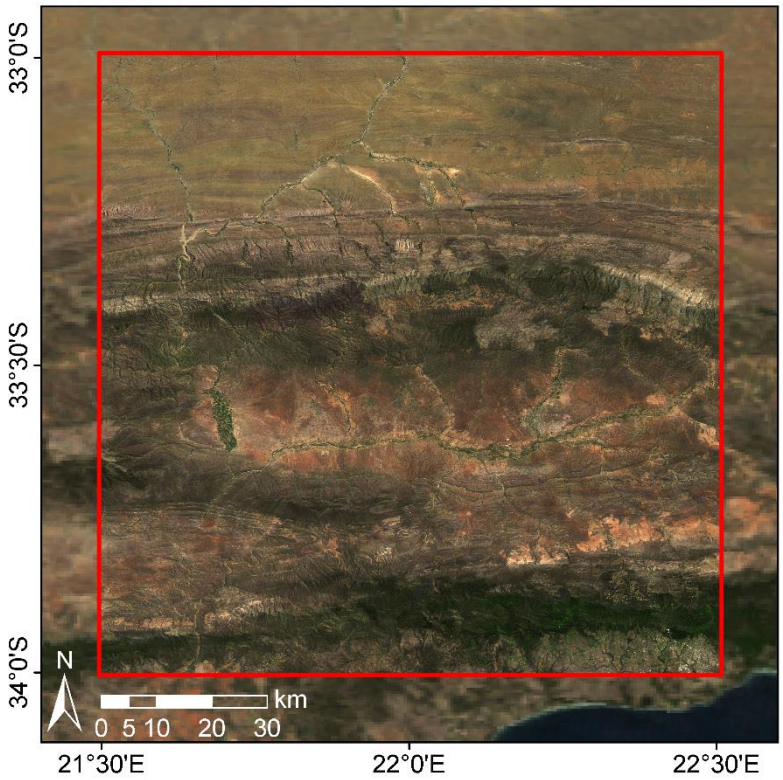

Figure 6. Homogenised mosaic on MODIS reference image background

Figure 7 (a) shows a close-up section of the DMC DN mosaic where a hot spot (i.e. a BRDF effect where sunlight is strongly reflected back into the camera) and seam lines between adjacent images are visible. Figure 7 (b) demonstrates the successful removal of the hot spot and seam lines after correction with the surface reflectance extraction method.

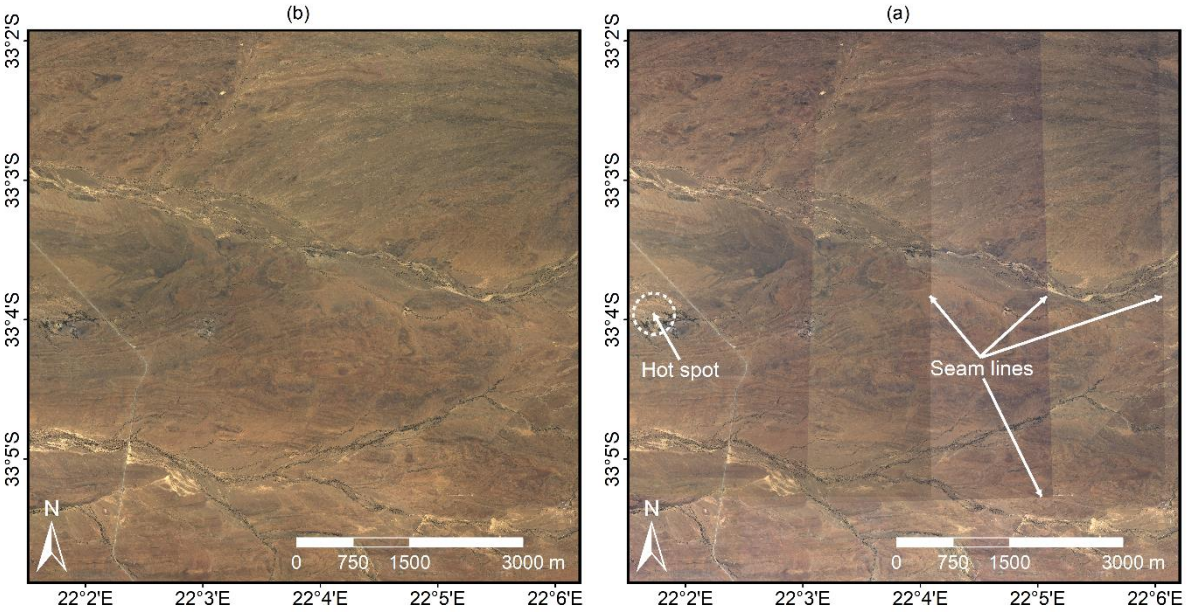

Figure 7. Reduction of hot spot and seam lines, with (a) showing raw DN images including hot spot and seam lines and (b) the corrected surface reflectance image

3.3 MODIS Statistical Comparison

Figure 8 shows scatter plots of the DMC DN and MODIS surface reflectance values with R^2 coefficients indicating correlation strength. Figure 9 shows similar scatter plots for the DMC and MODIS surface reflectance values. Differences in the MODIS and DMC surface reflectance values at MODIS resolution are in part due to the use of the cubic spline interpolation to upsample the **M** and **C** rasters from the MODIS to DMC resolution. The spline interpolation is non-invertible (i.e. downsampling the upsampled rasters does not produce the original **M** and **C** rasters, but successively smooths the data at each application). As indicated by Figure 8 and Figure 9, the correlation of the DMC and MODIS values is significantly improved when using the homogenised DMC surface reflectance rather than DN values. This improvement in correlation is not unexpected, as Figure 9 is effectively comparing calibrated values to the values that were used for calibration. Nevertheless, this comparison serves as a general check on the validity of the method and as an indication of the effect of spline interpolation between the disparate MODIS and DMC resolutions. MAD,

RMS and coefficient of determination statistics are given for the DMC and MODIS surface reflectance values in Table 1. Reflectance differences are the greatest in the NIR band, most likely due to the dissimilar MODIS and DMC RSRs in this band (Figure 2). This demonstrates the importance of using a reference image from a sensor with similar RSRs to those of the target imagery.

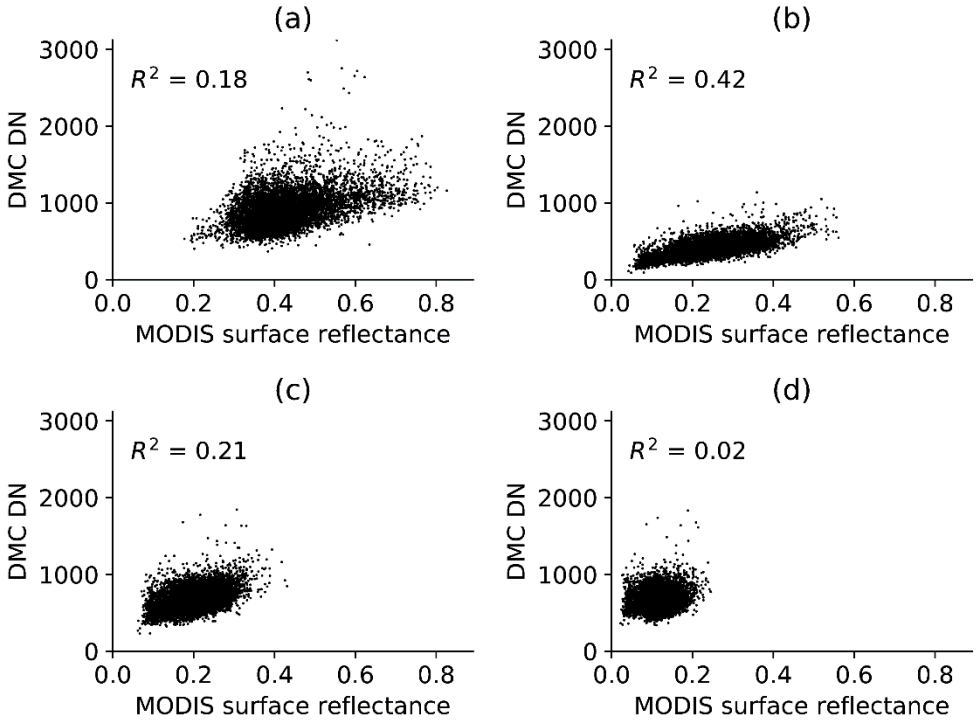

Figure 8. DMC DN values and MODIS surface reflectance correlation for the (a) NIR, (b) red, (c) green and (d) blue bands

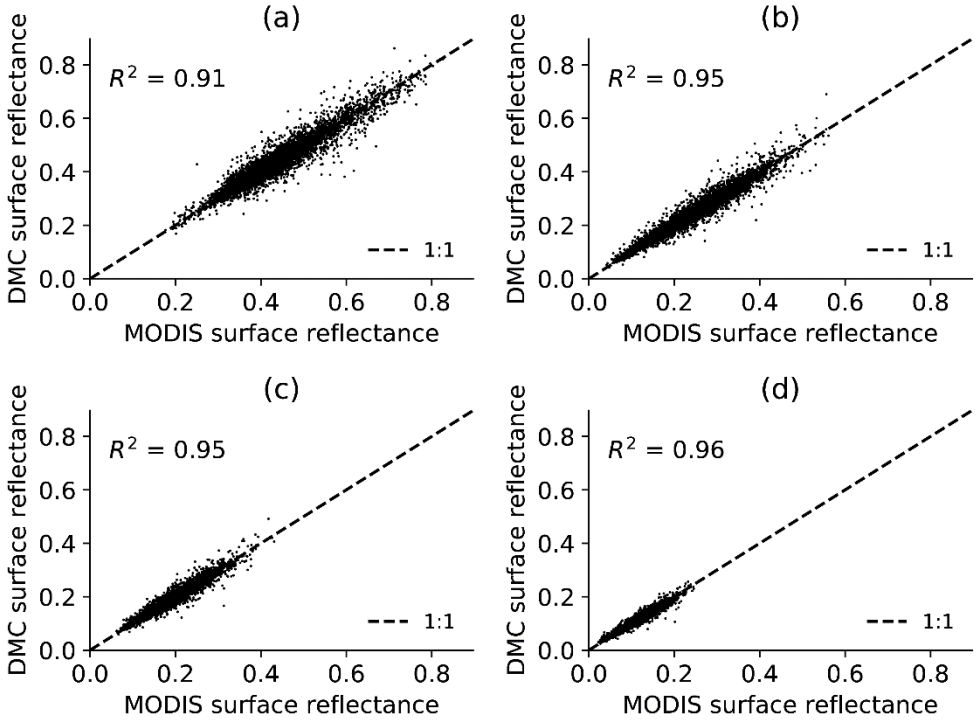

Figure 9. DMC homogenised mosaic and MODIS surface reflectance correlation for the (a) NIR, (b) red, (c) green and (d) blue bands

Table 1. Statistical comparison between MODIS and DMC surface reflectance images

Band	Mean absolute difference (%)	RMS (%)	R^2
Near-infrared	1.70	2.50	0.91
Red	1.18	1.75	0.95
Green	0.79	1.16	0.96
Blue	0.48	0.69	0.96
All	1.04	1.67	0.94

3.4 SPOT 5 Statistical Comparison

An indication of magnitude of discrepancies in the SPOT 5 image is shown in Table 2, which shows the statistics for the difference between the SPOT 5 and MODIS images. The relatively low mean overall absolute reflectance difference of 3.35% between the SPOT 5 and MODIS values is consequently a good indication that the SPOT 5 surface reflectance

extraction is effective. Note that the completeness of the SPOT 5 comparisons are limited by the missing blue band and partial coverage of the study area, as shown in Figure 3.

Statistics for the reflectance difference between the corrected SPOT 5 image and the DMC homogenised mosaic are shown in Table 3. Not all of the reflectance differences can be attributed to errors in the homogenised DMC surface reflectances. Spatial misalignment of pixels due to orthorectification differences and BRDF errors in the SPOT 5 surface reflectances also contribute to the recorded differences. Despite this uncertainty due to the contribution of other error sources, these reflectance differences compare well to figures reported by other aerial image correction methods. Collings et al. (2011) achieved RMS reflectance errors of 1.37%–12.30% measured on placed targets of known reflectance for their aerial mosaic correction technique, and in the aerotriangulation approach of López et al. (2011), mean absolute reflectance differences of approximately 3.30%–5.00% were obtained on field measured test sites distributed throughout their study area. Similarly to the MODIS comparison, the largest reflectance differences occur in the NIR band. Again, this is likely due to dissimilarities in the RSRs of MODIS, DMC and SPOT 5 sensor NIR bands (see Figure 2 and Figure 11).

Scatter plots of DMC DN and SPOT 5 surface reflectance values are shown in Figure 12, and DMC surface reflectance and SPOT 5 surface reflectance values are shown in Figure 13, with R^2 coefficients indicating correlation strength. The R^2 values show a moderately strong correlation of 0.84 averaged over the bands. The lack of perfect correlation is due to, among other error sources, the effect of small scale land cover heterogeneity and differing SPOT 5 and DMC RSRs. The SPOT 5-MODIS scatter plots in Figure 14 show similar deviations from the one-to-one line as those for SPOT 5-DMC in Figure 13, especially for

NIR. This suggests that the SPOT 5 image must be contributing, at least in part, to the SPOT 5-DMC differences. The effect of dissimilar SPOT 5, DMC and MODIS NIR RSRs is again evidenced in Figure 13 and Figure 14 as the marked deviations of the NIR scatters from the identity lines. Despite these disparities, the homogenisation of DMC surface reflectance provides a substantial improvement in correlation between the DMC and SPOT 5 values.

The effect of increasing the sliding window size on the reflectance difference between the SPOT 5 and DMC homogenised sub-sections is shown in Figure 15 (points are labelled with their corresponding window dimensions). The general characteristic is for the MAD to increase with sliding window size, suggesting that there is not an overfitting problem for small window sizes. The approximation of radiometric transfer and viewing geometry effects as locally linear relationships (Equations (5) and (12)) will be more precise for smaller sliding windows. As the sliding window size increases, the effective resolution of the radiometric homogenisation decreases, which likely results in the increasing MAD. This result supports the choice of a one pixel sliding window for the case study.

Comparisons of diagnostic SPOT 5 and DMC spectra are shown in Figure 16. These spectra were manually selected from single pixels in homogenous areas. There is a marked improvement in the similarity of the DMC and SPOT 5 surface reflectance values after homogenisation for these critical cases. The MAD and RMS difference of the SPOT 5 and DMC diagnostic reflectance spectra are 4.52% and 5.70% respectively. While not representative of wider variation, these values are similar to the ones produced by the statistical image analysis (see Table 3).

False colour CIR (colour-infrared) renderings of the DMC, SPOT 5 and difference images are shown in Figure 10. The contrast stretched difference image shows that most discrepancies occur in the rugged mountainous areas that extend west to east in the northern section of the scene and in densely vegetated areas along river banks in the southern section of the scene. No shadow or terrain correction was performed on the SPOT 5 image. Shadow variations occurring in the DMC images below the scale of the reference resolution are not accounted for by the proposed method. Disparities in the mountainous areas are mainly due to differing, uncorrected shadow effects likely caused by variations in the time of day when the images were captured (the aerial images were captured throughout the day, while the SPOT 5 image was captured at 10:29). A particularly bright area is noticeable in the upper right corner of the difference image. This corresponds to an area of bare ground that is bright in both the DMC and MODIS images and likely corresponds to a BRDF correction failure. It is not possible to say if this failure occurs in the SPOT 5 and/or DMC corrections. The differences in the densely vegetated and cultivated areas are attributed to the differences in the MODIS, DMC and SPOT 5 sensor NIR RSRs being amplified by the known high NIR reflectivity of vegetation. Abrupt changes in BRDF may occur between adjacent fields in cultivated areas along the major rivers. As discussed in Section 2.2, these changes may not be captured at the MODIS resolution and could also be contributing to the NIR differences in these regions.

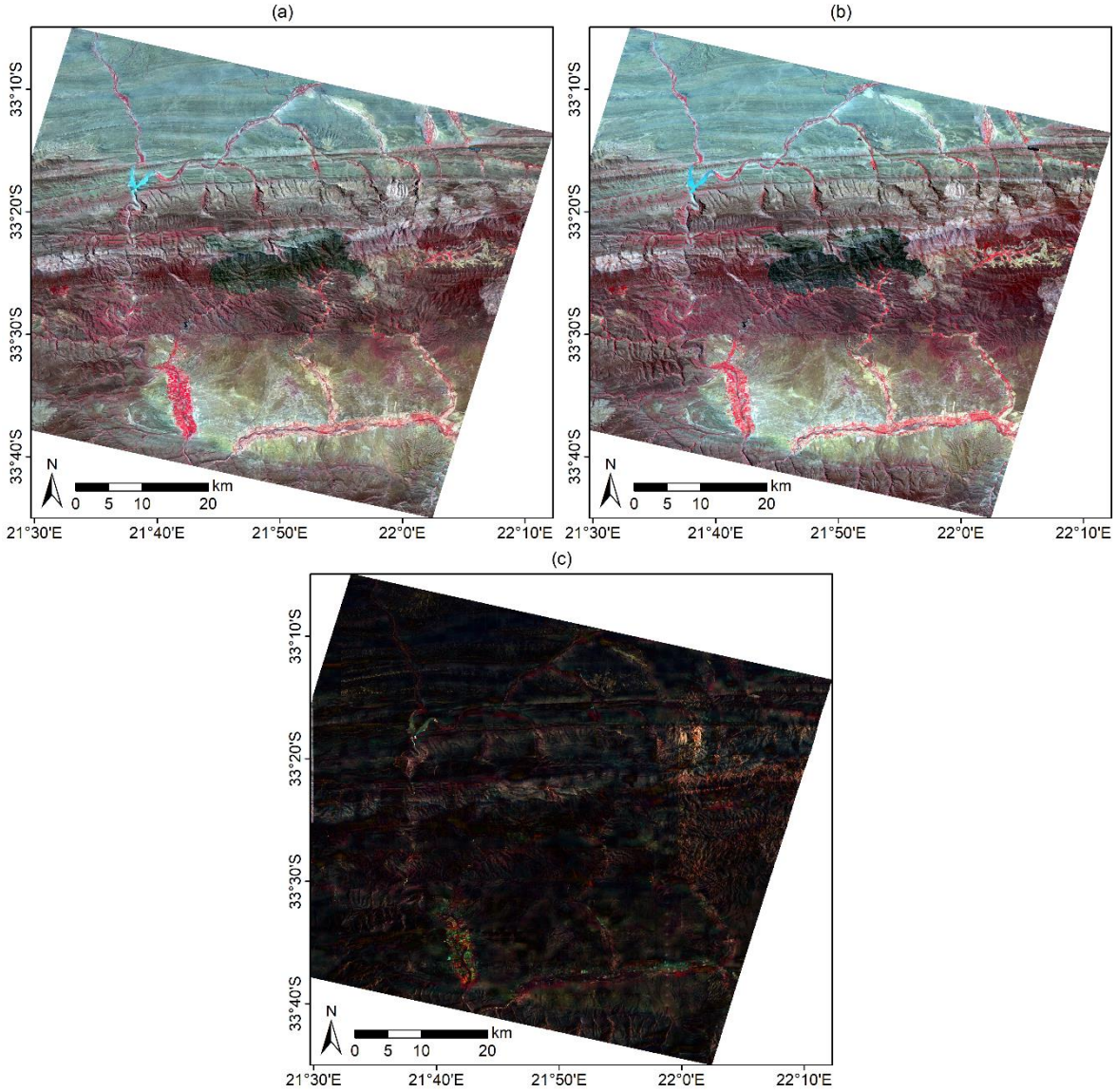

Figure 10. DMC and SPOT 5 surface reflectance comparison with (a) DMC homogenised mosaic masked to SPOT 5 extent; (b) SPOT 5 surface reflectance image; and (c) contrast stretched absolute difference image

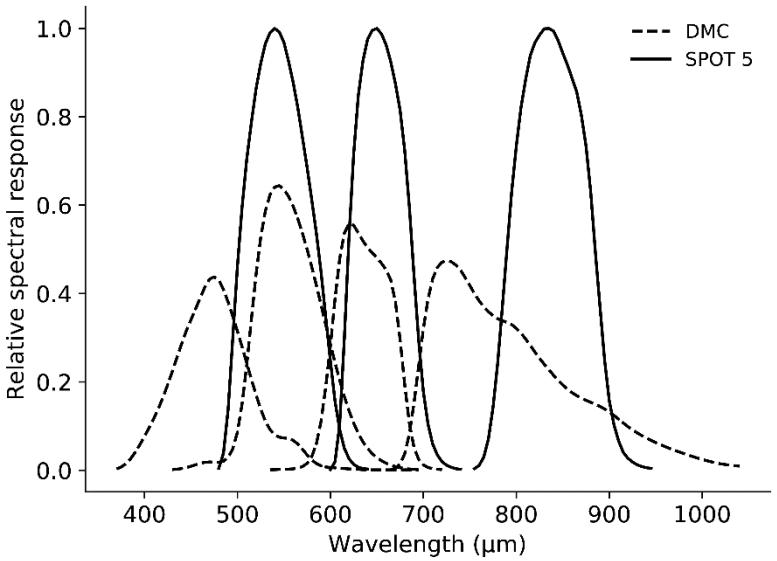

Figure 11. DMC and SPOT 5 RSRs

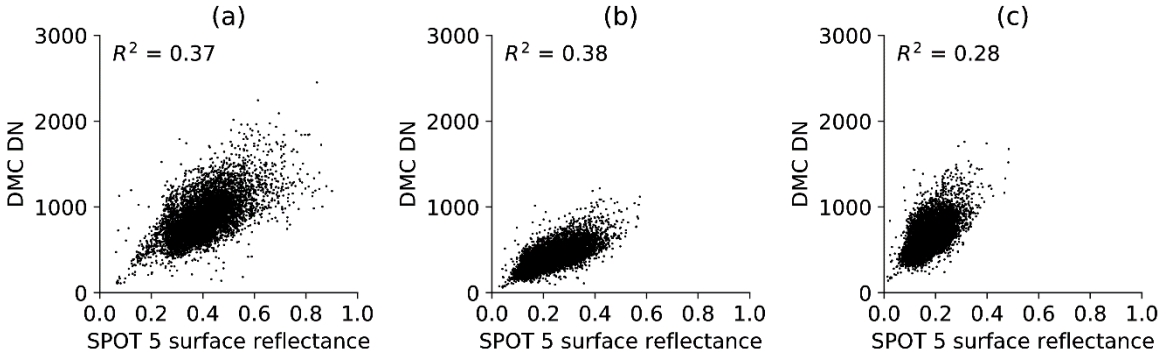

Figure 12. DMC DN mosaic and SPOT 5 surface reflectance correlation for the (a) NIR, (b) red and (c) green bands

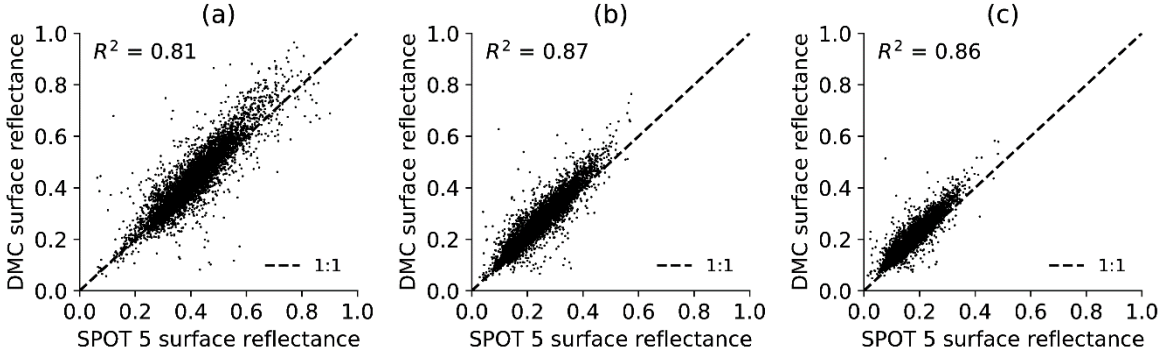

Figure 13. DMC homogenised mosaic and SPOT 5 surface reflectance correlation for the (a) NIR, (b) red and (c) green bands

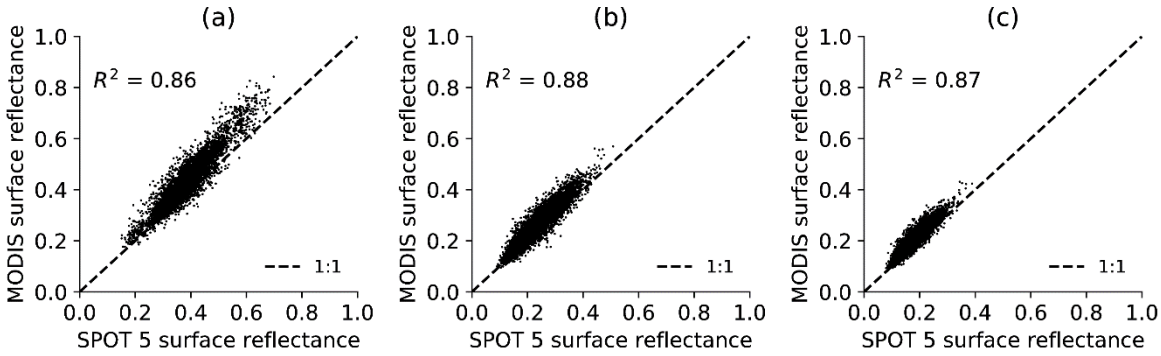

Figure 14. MODIS and SPOT 5 surface reflectance correlation for the (a) NIR, (b) red and (c) green bands

Table 2. Statistical comparison between SPOT 5 and MODIS surface reflectance images

Band	Mean absolute difference (%)	RMS (%)	R^2
Near-infrared	4.81	5.79	0.86
Red	2.83	3.55	0.88
Green	2.40	2.91	0.87
All	3.35	4.27	0.87

Table 3. Statistical comparison between SPOT 5 and DMC surface reflectance images

Band	Mean absolute difference (%)	RMS (%)	R^2
Near-infrared	4.00	5.66	0.80
Red	3.11	4.27	0.86
Green	3.19	3.86	0.85
All	3.43	4.66	0.84

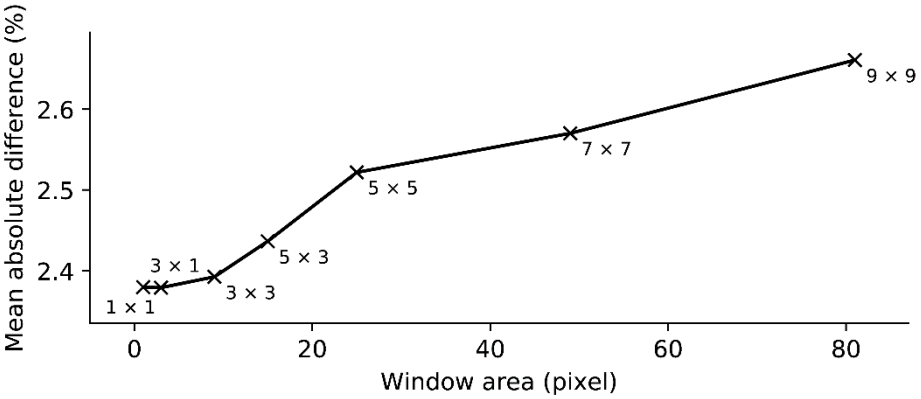

Figure 15. Effect of sliding window size on SPOT 5 comparison

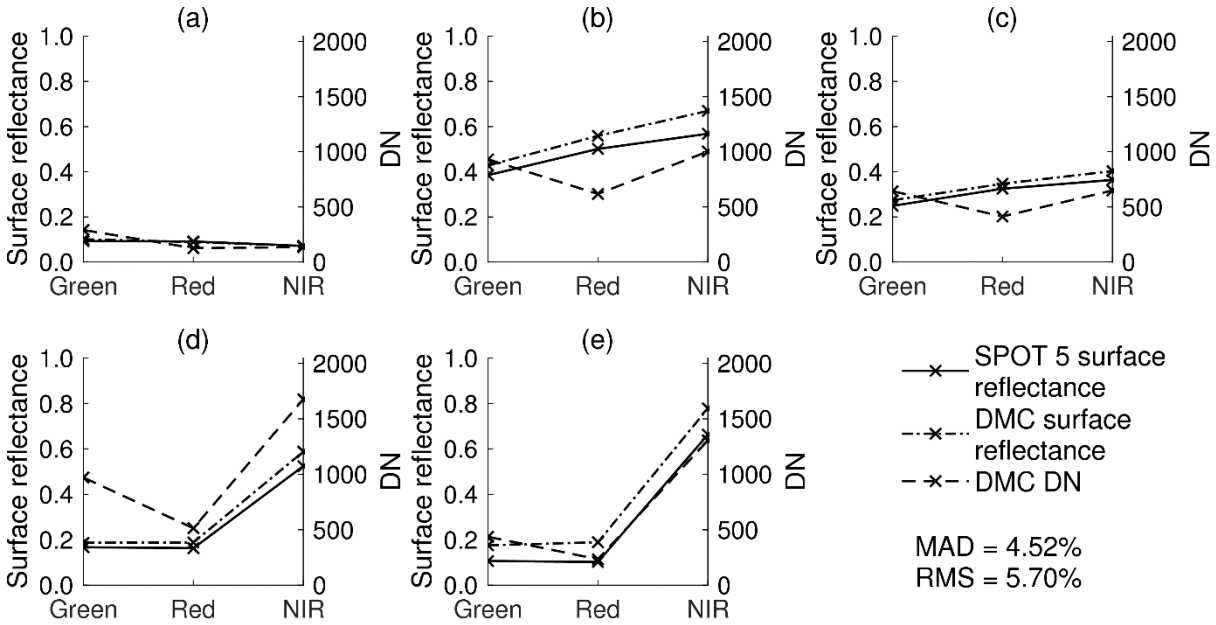

Figure 16. Comparison of DMC and SPOT 5 spectra for (a) water, (b) bright sand, (c) bare ground, (d) vegetation type 1 and (e) vegetation type 2 surfaces

4 Conclusions

This study proposes a method of homogenising surface reflectance in aerial imagery by calibrating to a coarse-resolution, concurrent and collocated satellite image that has already been corrected for atmospheric and BRDF effects. It is shown that a spatially varying linear model can be used to approximate the relationship between the DN measured by the aerial sensor and the surface reflectance of the satellite image. The parameters of the model are estimated for each satellite pixel location using least squares regression inside a small sliding

window. The method is limited by the low resolution of the satellite reference image. The effects of viewing geometry and land cover variations below the scale of a reference pixel are averaged out. Only gradual BRDF and atmospheric variations that can be captured by the coarser resolution of the reference image are compensated for.

The proposed surface reflectance homogenisation method was applied to 2228 Intergraph DMC images covering an area 96 km × 107 km in size, omitting the offset parameter, *C*, from the model. A MODIS MCD43A4 NBAR product was used as the surface reflectance reference. The DMC homogenised mosaic was free of visible seam lines and hot spots and matched the MODIS reference well. The DMC homogenised mosaic was also compared to a concurrent SPOT 5 image in order to establish the method's efficacy at a spatial resolution closer to that of the DMC source resolution than the MODIS reference. The SPOT 5 image was corrected for atmospheric effects and converted to surface reflectance using the ATCOR 3 method. The mean R^2 value and the mean absolute reflectance difference between the DMC mosaic and SPOT 5 image were 0.84 and 3.43% respectively. Despite the limitations and approximations inherent in the method, these statistics are considered supportive of the method's efficacy and are similar to figures reported by Collings et al. (2011) and López et al. (2011) for related correction techniques. While the method was evaluated on aerial imagery, it is not limited to this type of data and could be applied to any multi-spectral VHR imagery, including satellite and unmanned aerial vehicle (UAV) imagery.

The proposed technique does not require explicit BRDF and atmospheric correction; and mosaic normalisation techniques to reduce seam lines are not necessary. The spatially varying linear model allows for flexibility in the BRDF characteristics that can be corrected

for. The method accuracy is limited by the accuracy of the reference surface's reflectance i.e. the accuracy of the homogenised images can at best be that of the MODIS reference. The method is also limited by the need for a reference image concurrent and spectrally similar to the aerial imagery. Such an image may not always be obtainable. The MODIS and DMC RSRs are quite different in the near-infrared region of the spectrum (see Figure 2). The surface reflectance homogenisation method approximates the effect of different sensor spectral responses with a linear relationship that is contained by the model of Equation (5). This approximation was supported by a simulation of MODIS and DMC measurements for typical land cover spectra. The relatively higher (4%) NIR reflectance difference between the DMC mosaic and the SPOT 5 values, and discrepancies in vegetated areas, are likely due to the more exaggerated differences in NIR RSRs between the MODIS, DMC and SPOT sensors.

While the results of the surface reflectance homogenisation technique were surprisingly good given the simplicity of the method, some aspects warrant further investigation. The effects of including the offset parameter, *C* should be investigated. The offset parameter may improve homogenised results where atmospheric effects like haze are relatively severe. Local terrain effects are poorly represented at the MODIS resolution. Landsat surface reflectance offers a higher resolution alternative but has the drawback of no BRDF correction (Schmidt et al. 2012). It could nevertheless be a useful homogenisation reference, as it will exhibit less BRDF variation than low altitude aerial imagery due to its narrower FOV. The MISR instrument is also a promising alternative to MODIS. MISR RSRs are a better match to those of the Intergraph DMC than the MODIS bands, and it is possible to obtain 275 m reflectance products using MISR-HR (Verstraete et al. 2012). The MISR instrument captures data at nine different angles, which allows a more accurate

modelling of the BRDF compared to the kernel-based approach followed in the calibration of the MODIS data (Strahler and Muller 1999). It would be informative to test the performance of the method with Landsat and MISR surface reflectance reference images.

Acknowledgements

We would like to thank Jan Vlok for proposing the vegetation mapping study that led to this research and for assistance in selecting the study area, Adrian Roos and Intergraph South Africa for providing a licence for Intergraph PPS, Bernard Jacobs of Geospace International for assistance in understanding the NGI image processing workflow and in obtaining DMC RSR data, Theo Pauw and Garth Stephenson of CGA for assistance with computing and software resources, Julie Verhulp and NGI for provision of the aerial imagery and www.linguafix.net for language editing. This work was supported by funding from the Gamtoos Irrigation Board (GIB). GIB was otherwise not involved in this research. The financial assistance of the National Research Foundation (NRF) towards this research is hereby acknowledged. Opinions expressed and conclusions arrived at, are those of the authors and are not necessarily to be attributed to the NRF.

References

Akhmanov, S. A., and S. Yu. Nikitin. 1997. *Physical Optics*. Oxford: Clarendon Press.

Baldridge, A. M., S. J. Hook, C. I. Grove, and G. Rivera. 2009. "The ASTER Spectral Library Version 2.0." *Remote Sensing of Environment* 113 (4). Elsevier Inc.: 711–715. doi:10.1016/j.rse.2008.11.007.

Berk, A., G. P. Anderson, L. S. Bernstein, P. K. Acharya, H. Dothe, M. W. Matthew, S. M. Adler-Golden, et al. 1999. "MODTRAN4 Radiative Transfer Modeling for Atmospheric Correction." In *Proceedings of SPIE - The International Society for Optical Engineering*, 3756:348–353. Denver, CO: Society of Photo-Optical Instrumentation Engineers.

Chandelier, Laure, and Gilles Martinoty. 2009. "A Radiometric Aerial Triangulation for the

Equalization of Digital Aerial Images and Orthoimages." *Photogrammetric Engineering & Remote Sensing* 75 (2): 193–200.

Chander, Gyanesh, D.J. Meyer, and D.L. Helder. 2004. "Cross Calibration of the Landsat-7 ETM+ and EO-1 ALI Sensor." *IEEE Transactions on Geoscience and Remote Sensing* 42 (12): 2821–2831. doi:10.1109/TGRS.2004.836387.

Collings, Simon, Peter Caccetta, Norm Campbell, and Xiaoliang Wu. 2011. "Empirical Models for Radiometric Calibration of Digital Aerial Frame Mosaics." *IEEE Transactions on Geoscience and Remote Sensing* 49 (7): 2573–2588. doi:10.1109/TGRS.2011.2108301.

Downey, Michael, Robert Uebbing, Stephan Gehrke, and Ulrich Beisl. 2010. "Radiometric Processing of ADS Imagery: Using Atmospheric and BRDF Corrections in Production." In *ASPRS 2010 Annual Conference*. San Diego, CA, USA.

Gao, Caixia, Xiaoguang Jiang, Xianbin Li, and Xiaohui Li. 2013. "The Cross-Calibration of CBERS-02B/CCD Visible-near Infrared Channels with Terra/MODIS Channels." *International Journal of Remote Sensing* 34 (9–10): 3688–3698. doi:10.1080/01431161.2012.716531.

GDAL Development Team. 2014. "Geospatial Data Abstraction Library." *Open Source Geospatial Foundation*. http://www.gdal.org/.

Gehrke, S., and B. T. Beshah. 2016. "Radiometric Normalization of Large Airborne Image Data Sets Acquired by Different Sensor Types." *International Archives of the Photogrammetry, Remote Sensing and Spatial Information Sciences - ISPRS Archives* 2016–Janua (July): 317–326. doi:10.5194/isprsarchives-XLI-B1-317-2016.

Gehrke, Stephan. 2010. "Radiometric Processing of ADS Imagery: Mosaicking of Large Image Blocks." In *Opportunities for Emerging Geospatial Technologies*, 1:184–195. American Society for Photogrammetry and Remote Sensing Annual Conference 2010

Held 26-30 April 2010. San Diego, USA: American Society for Photogrammetry and Remote Sensing.

Honkavaara, Eija, Roman Arbiol, Lauri Markelin, Lucas Martinez, Michael Cramer, Stéphane Bovet, Laure Chandelier, et al. 2009. “Digital Airborne photogrammetry—A New Tool for Quantitative Remote sensing?—A State-of-the-Art Review on Radiometric Aspects of Digital Photogrammetric Images.” *Remote Sensing* 1 (4): 577–605. doi:10.3390/rs1030577.

Hou, Hsieh S., and H. Andrews. 1978. “Cubic Splines for Image Interpolation and Digital Filtering.” *IEEE Transactions on Acoustics, Speech, and Signal Processing* 26 (6): 508–517. doi:10.1109/TASSP.1978.1163154.

Jiang, G. M., and Z. L. Li. 2009. “Cross-Calibration of MSG1-SEVIRI Infrared Channels with Terra-MODIS Channels.” *International Journal of Remote Sensing* 30 (3): 753–769. doi:10.1080/01431160802392638.

Lelong, Camille C. D., Phillipe Burger, Guillame Jubelin, Bruno Roux, Sylvain Labbé, and Frédéric Baret. 2008. “Assessment of Unmanned Aerial Vehicles Imagery for Quantitative Monitoring of Wheat Crop in Small Plots.” *Sensors* 8 (5): 3557–3585. doi:10.3390/s8053557.

Li, Lili, Jingxue Yang, and Yunpeng Wang. 2012. “Cross-Calibration of HJ-1B/CCD1 Image Based on Aqua/MODIS Data.” In *2012 Second International Workshop on Earth Observation and Remote Sensing Applications*, 116–119. Shanghai, China: IEEE. doi:10.1109/EORSA.2012.6261147.

Liu, J.-J., Z. Li, Y.-L. Qiao, Y.-J. Liu, and Y.-X. Zhang. 2004. “A New Method for Cross-Calibration of Two Satellite Sensors.” *International Journal of Remote Sensing* 25 (23): 5267–5281. doi:10.1080/01431160412331269779.

López, David Hernández, Beatriz Felipe García, José González Piqueras, and Villa Alcázar

Guillermo. 2011. “An Approach to the Radiometric Aerotriangulation of Photogrammetric Images.” *ISPRS Journal of Photogrammetry and Remote Sensing* 66 (6): 883–893. doi:10.1016/j.isprsjprs.2011.09.011.

Manabe, Syukuro, and Robert F. Strickler. 1964. “Thermal Equilibrium of the Atmosphere with a Convective Adjustment.” *Journal of the Atmospheric Sciences* 21 (4): 361–385. doi:10.1175.

Markelin, Lauri, Eija Honkavaara, Daniel Schläpfer, Stéphane Bovet, and Ilkka Korpela. 2012. “Assessment of Radiometric Correction Methods for ADS40 Imagery.” *Photogrammetrie - Fernerkundung - Geoinformation* 2012 (3): 251–266. doi:10.1127/1432-8364/2012/0115.

MODIS Land Team. 2014. “EOS Validation Status for MODIS BRDF/albedo: MCD43.” http://tinyurl.com/jyx8gjs.

Richter, R. 1997. “Correction of Atmospheric and Topographic Effects for High Spatial Resolution Satellite Imagery.” *International Journal of Remote Sensing* 18 (5): 1099–1111.

Roujean, Jean-Louis, Marc Leroy, and Pierre-Yves Deschamps. 1992. “A Bidirectional Reflectance Model of the Earth’s Surface for the Correction of Remote Sensing Data.” *Journal of Geophysical Research* 97 (D18): 20455. doi:10.1029/92JD01411.

Schaepman-Strub, G., M.E. Schaepman, T.H. Painter, S. Dangel, and J.V. Martonchik. 2006. “Reflectance Quantities in Optical Remote Sensing—definitions and Case Studies.” *Remote Sensing of Environment* 103 (1): 27–42. doi:10.1016/j.rse.2006.03.002.

Schmidt, G., C. Jenkerson, J. Masek, E. Vermote, and F. Gao. 2012. *Landsat Ecosystem Disturbance Adaptive Processing System (LEDAPS) Algorithm Description*. doi:No. 2013-1057.

Strahler, A. H., and J. P. Muller. 1999. “MODIS BRDF Albedo Product : Algorithm

Theoretical Basis Document." *MODIS Product ID: MOD43*. NASA. doi:http://duckwater.bu.edu/lc/mod12q1.html.

Van Niekerk, A. 2014. "Stellenbosch University Digital Elevation Model (SUDEM)." *ResearchGate* 16 (February 2016). doi:10.13140/2.1.3015.5922.

Vermote, E., D. Tanre, J.L. Deuze, Maurice Herman, and J.-J. Morcette. 1997. "Second Simulation of the Satellite Signal in the Solar Spectrum, 6S: An Overview." *IEEE Transactions on Geoscience and Remote Sensing* 35 (3): 675–686. doi:10.1109/36.581987.

Vermote, E, D Tanré, J L Deuzé, and M Herman. 2006. *Second Simulation of a Satellite Signal in the Solar Spectrum - Vector (6SV) (User Guide V3)*. NASA.

Verstraete, Michel M., Linda A. Hunt, Robert J. Scholes, Marco Clerici, Bernard Pinty, and David L. Nelson. 2012. "Generating 275-M Resolution Land Surface Products from the Multi-Angle Imaging Spectroradiometer Data." *IEEE Transactions on Geoscience and Remote Sensing* 50 (10): 3980–3990. doi:10.1109/TGRS.2012.2189575.

Vicente-Serrano, S, F Pérez-Cabello, and T Lasanta. 2008. "Assessment of Radiometric Correction Techniques in Analyzing Vegetation Variability and Change Using Time Series of Landsat Images." *Remote Sensing of Environment* 112 (10): 3916–3934. doi:10.1016/j.rse.2008.06.011.

Webb, Andrew R. 2002. *Statistical Pattern Recognition*. Chichester, UK: John Wiley & Sons, Ltd. doi:10.1002/0470854774.

List of Figures

List of Tables